

Nanoscale

Accepted Manuscript



This is an *Accepted Manuscript*, which has been through the Royal Society of Chemistry peer review process and has been accepted for publication.

Accepted Manuscripts are published online shortly after acceptance, before technical editing, formatting and proof reading. Using this free service, authors can make their results available to the community, in citable form, before we publish the edited article. We will replace this *Accepted Manuscript* with the edited and formatted *Advance Article* as soon as it is available.

You can find more information about *Accepted Manuscripts* in the [Information for Authors](#).

Please note that technical editing may introduce minor changes to the text and/or graphics, which may alter content. The journal's standard [Terms & Conditions](#) and the [Ethical guidelines](#) still apply. In no event shall the Royal Society of Chemistry be held responsible for any errors or omissions in this *Accepted Manuscript* or any consequences arising from the use of any information it contains.

ARTICLE

Kinetically-controlled growth of cubic and octahedral Rh-Pd alloy oxygen reduction electrocatalysts with high activity and durability

Cite this: DOI: 10.1039/x0xx00000x

Received 00th January 2012,
Accepted 00th January 2012

DOI: 10.1039/x0xx00000x

www.rsc.org/

Yucong Yan,^{a,§} Fangwei Zhan,^{a,§} Jingshan Du,^a Yingying Jiang,^a Chuanhong Jin,^a Maoshen Fu,^b Hui Zhang,^{a,*} and Deren Yang^a

Rh is a promising candidate as an indispensable component in bimetallic catalysts due to its unique capability to resist against the aggressive corrosion from the reaction medium. However, Rh has too strong oxygen binding ability and is generally not suitable for oxygen reduction reaction (ORR). Here, we have demonstrated shape-controlled synthesis of Rh-Pd alloy nanocrystals with high activity and durability for ORR by retarding the reaction kinetics under an ultra-slow injection rate of metal salts using a syringe pump. Under precise control on sluggish reaction kinetics, Pd followed a preferential overgrowth along the <100> direction, whereas, the growth behavior of Rh was dominant along the <111> direction. These different kinetically-controlled growth behaviors associated with Rh and Pd were essential for achieving the shape transition between cube and octahedron of their alloys. The Rh₈Pd₉₂ alloy octahedra exhibited the highest mass activity with a value of 0.18 mA/μg in term of the equivalent Pt cost, and were two-fold high as that of commercial Pt/C. Significantly, all Rh-Pd alloy nanocrystals were highly stable with only less than 25% loss in mass activity after 30,000 CV cycles in O₂ saturated acid solution compared to ~56% loss of the commercial Pt/C (E-TEK). Indeed, the mass activity of Rh₈Pd₉₂ showed 3.3 times high as that of commercial Pt/C after the accelerated stability test (ADT). This improvement in activity and durability may arise possibly from synergistic effects between facet and surface composition.

Introduction

Many catalytic reactions are well-known to be very sensitive to the surface structure of noble-metal nanocrystals in a catalyst.^[1-3] It is clear that the surface geometry of a noble-metal nanocrystal is strongly affected by its shape, which determines surface atoms at facets, edges, and corners.^[4-7] As such, colloidal based shape control offers a powerful and versatile means to tailor surface of noble-metal nanocrystals as well as its reactivity and selectivity for a rich variety of catalytic reactions such as oxygen electro-reduction reaction (ORR). For example, it is demonstrated that the extended Pt₃Ni{111} surface exhibited over 8-fold more active than its {100} surface in ORR specific activity.^[8] The improvement in ORR activity was also achieved in the Pt₃Ni octahedral nanocrystals enclosed by the {111} facets as compared with the corresponding cubes covered by the {100} facets.^[9,10] This type of facet sensitivity has also received unremitting interested as an ideal platform and been applied in various catalytic reactions over the past decade.^[11-13] In general, capping agent is a commonly-used for shape-controlled synthesis by changing surface energy via selective adsorption and their growth rates.^[14,15] Thus, a capping agent could stabilize some specific facets during

thermodynamically-controlled crystal growth (e.g. PVP for Ag{100} and citrate for Ag{111} surface).^[17-21] However, the use of different capping agents to control the shape of noble-metal nanocrystals severely interferes the results of structure-dependent properties due to the residual of adsorbates with different chemical features on the surface of such nanocrystals.^[22,23]

Recently, kinetic control has emerged as a promising approach to shape-controlled synthesis of noble-metal nanocrystals in a solution.^[24,25] In practice, several groups found that dramatically slowing down the growth rate of nanocrystals might substantially alter their original growth behavior of nanocrystals, and thus control the shape for a given metal due to a manipulation of its reaction kinetics.^[26-28] For example, the formation of PdBr₄²⁻ complex favored the formation of Pd{111} dominant shapes, including octahedron and plate, under kinetic control, although thermodynamically Br⁻ ions could stabilize the {100} facets serving as a capping agent.^[29] Most recently, Xia et al. have further extended the capability of this approach to achieve nucleation and growth of Ag on one, three, and six of the equivalent {100} faces on a cubic Pd seed by manipulating the injection rate of AgNO₃.^[30]

Despite enormous success, maneuvering the shape of noble metals by precisely controlling the reaction kinetics still remains a great challenge, especially for a system involving bimetallic alloys.

Here, we report a facile polyol approach to achieve shape and composition-controlled Rh-Pd alloy cubes and octahedra by simultaneously injecting Rh and Pd salt precursors with an extremely slow rate (e.g., 2 mL/h) using a syringe pump. We found that the different kinetically-controlled growth behaviors associated with Rh and Pd at an extremely slow feeding rate was essential for achieving this shape transition phenomenon. Shape controlled Pd-based alloys have been studied as alternative non-Pt ORR catalysts due to relatively less expensive price and more abundant reserve as well as similar electronic properties to Pt.^[31-33] The incorporation of Rh with a unique capability to resist against acid etching into Pd-based catalysts could enhance their activity and durability for ORR due to a possible synergistic effect between these two metals.^[34-37]

Experimental section

Chemicals and Materials. Sodium hexachlororhodate (Na_3RhCl_6 , Sigma-Aldrich, 97%), sodium tetrachloropalladate (Na_2PdCl_4 , Sigma-Aldrich, 99.998%), potassium bromide (KBr, Sinopharm Chemical Reagent Co. Ltd), poly(vinyl pyrrolidone) (PVP, MW \approx 40000, Sigma-Aldrich), ascorbic acid (AA, Sigma-Aldrich), ethylene glycol (EG), acetone, and ethanol (Sinopharm Chemical Reagent Co. Ltd) were all used as received. The type of syringe was plastic (10 mL, Hangzhou Longde Medical Apparatus Co., Ltd.) All syntheses were carried out in glass vials (25 mL, Shuniu).

Synthesis of Rh-Pd cubes and octahedrons. Rh-Pd cubes were synthesized by injecting a mixed EG solution of Na_3RhCl_6 and Na_2PdCl_4 into another EG solution containing PVP, AA and KBr using a syringe pump. In a standard synthesis, a 6.0 mL of EG containing 111 mg PVP, 60 mg AA, and 500 mg KBr was added to a vial, and pre-heated to 110 °C in an oil bath under magnetic stirring for 30 min and then ramp to 140 °C. Subsequently, a 5.0 mL of EG containing 38 mg Na_3RhCl_6 and 30 mg Na_2PdCl_4 with a Rh/Pd molar ratio of 1:1 was injected simultaneously into the pre-heated vial through a syringe pump at a injection rate of 2 mL/h. The reaction was allowed to proceed for 2.5 h at 140 °C. The product was collected by centrifugation, washed three times with acetone to remove excess PVP, KBr, AA, and re-dispersed in ethanol. In addition, Rh-Pd octahedrons were synthesized by decreasing the temperature of reaction to 120 °C with all other parameters being the same as in the standard procedure. We also systematically investigated the effects of the molar ratio (e.g., 4:1, 2:1, 2:1, 4:1) of Na_3RhCl_6 and Na_2PdCl_4 fed into the reaction, the duration of reaction as well as the injection rate on the final morphology of resultant Rh-Pd alloy nanocrystals at 140 and 120 °C, respectively.

Preparation of Carbon-Supported Catalysts. Carbon black (Vulcan XC-72) was used as support for making Rh-Pd catalysts (RhPd/C) according to a previous report with some minor modifications. In a standard preparation, carbon black particles were dispersed in ethanol and sonicated for 30 min. A designed amount of Rh-Pd alloy nanocrystals were added to this dispersion with a Rh-Pd/C mass ratio of 20:80. This

mixture was further sonicated for 10 min and stirred for 12 h. The resultant solids were precipitated out by centrifugation with ethanol.

Morphological, Structural, and Elemental Characterizations.

The obtained samples were characterized by X-ray powder diffraction (XRD) using a Rigaku D/max-ga x-ray diffractometer with graphite monochromatized Cu K α radiation ($\lambda = 1.54178 \text{ \AA}$). Transmission electron microscopy (TEM) images of the obtained samples were taken using a Philips CM 200 microscope operated at 160 kV. High-resolution transmission electron microscopy (HRTEM) was performed using a FEI Tecnai F30 G2 microscope operated at 300 kV. High-angle annular dark-field scanning TEM (HAADF-STEM) and Energy dispersive X-ray (EDX) mapping analyses were taken on a Cs-corrected STEM (TitanG2 80-200 ChemiSTEM equipped with a Super-X EDX detector system), operated at 200 kV using a probe with 50 pA beam current and a converge angle of 21.4 mrad. X-Ray Photoelectron Spectrometer (XPS) was performed on ESCALAB 250Xi (Thermo U.K.).

Electrochemical Measurements. A three-electrode cell was used to measure the electrochemical performances of Rh-Pd/C catalysts including the commercial Pt/C (ETEK). A glassy-carbon rotating disk electrode (RDE) was used as the working electrode (area: $\sim 0.196 \text{ cm}^2$). A 1 cm^2 platinum foil and a HydroFlex hydrogen electrode were used as the counter electrode and the reference. The reference electrode was placed in a separate compartment connected with main cell via a salt bridge. The hydrogen reference electrode was calibrated before all the tests via Hydrogen evolution reaction (HER). All potentials were referenced to the reversible hydrogen electrode (RHE). The electrolyte for cyclic voltammetry (CV) measurement and linear scan voltammetry (LSV) test for oxygen reduction reaction (ORR) was 0.1-M HClO_4 solution, diluted from 70% double-distilled perchloric acid (GFS Chemicals, USA) with Millipore ultrapure water (18.2 M Ω). To make catalyst ink, 5 mg of Rh-Pd/C catalysts was dispersed in 10 mL of a mixed solvent and sonicated for 10 min. The solvent contained a mixture of de-ionized water, isopropanol, and 5% Nafion 117 solution at the volumetric ratio of 8:2:0.05. 40 μL of the catalyst ink was added onto the RDE and dried under the air flow for 30 min to make the working electrode. The loading amount of Rh-Pd alloy catalysts on the RDE was determined to be $\sim 20 \mu\text{g}_{\text{metal}}/\text{cm}^2$. The electrochemical active surface area (ECSA) was determined from the CV curves, calculating the amount of charges by integrating hydrogen desorption region after double layer correction. The CV measurement was carried in argon-saturated 0.1 M HClO_4 solution at room temperature with a scan rate of 50 mV/s. ORR LSV curves were measured at the rotating rate of 1600 rpm in a 0.1-M HClO_4 solution, which was purged with oxygen for 30 min prior to, and during testing. The scan rate for ORR measurement was set at 10 mV/s. Data were used without iR-drop correction. The accelerated stability test (ADT) was carried out between 0.6 V and 1.0 V at a scan rate of 100 mV/s⁻¹ for 30,000 cycles in oxygen saturated 0.1-M HClO_4 solution.

Results and discussion

This synthesis is based on a modified polyol process that involves the simultaneous injection of Na_3RhCl_6 and Na_2PdCl_4

using a syringe pump at a rate of 2 mL/h into ethylene glycol (EG) with ascorbic acid (AA) and Br^- ions serving as reducing and capping agents, respectively. Using this strategy, Rh-Pd alloy cubes and octahedra with different compositions were successfully produced by varying the reaction temperature and molar ratios of Rh to Pd salt precursor fed into the reaction (see Figure 1). From this schematic illustration, it is clear that the Rh-rich samples preferred to take a cubic shape, whereas, the Pd-rich ones were dominated by a shape of octahedron despite different reaction temperatures (e.g., 140 and 120 °C). When the molar ratio of Rh to Pd precursors was kept to 1:1, however, the reaction temperature had a great influence in the shape of the resultant Rh-Pd alloy nanocrystals. In this case, Rh-Pd alloy cubes and octahedra were successfully produced at 140 and 120 °C, respectively. This shape evolution with the molar ratio of Rh to Pd precursor and reaction temperature can be attributed to different growth behavior associated with Rh and Pd at an extremely slow injection rate under kinetic control.

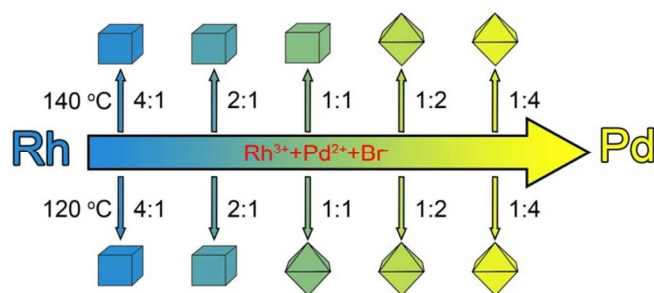


Figure 1. Schematic illustration showing the shape evolution of Rh-Pd alloy cubes and octahedra with the molar ratio of Rh to Pd salt precursors supplied in the reaction at 140 and 120 °C, respectively.

We fully characterized the morphology, structure, and composition of these Rh-Pd alloy nanocrystals by various techniques. Figure 2 shows transmission electron microscopy (TEM), high angle annular dark field scanning transmission electron microscopy (HAADF-STEM), energy dispersive X-ray (EDX), and high-resolution TEM (HRTEM) images of the Rh-Pd alloy nanocrystals that were prepared with a Rh/Pd molar ratio of 1:1 at an injection rate of 2 mL/h and 140 °C (denoted as the standard procedure in Supporting information). From the TEM image (Figure 2A), most of the Rh-Pd nanocrystals (ca. 80%) exhibited a shape of cube with an edge length of about 15 nm. The magnified TEM image (inset of Figure 2A) shows that the cube was slightly truncated at eight corners but mainly bounded by the {100} facets. The cubic shape of Rh-Pd nanocrystals was also revealed by the HAADF-STEM image (Figure 2B). The representative HRTEM image (Figure 2C) of an individual Rh-Pd cube recorded along the $\langle 001 \rangle$ zone axis (see FFT in Figure S1) clearly shows well-resolved, continuous fringes in the same orientation, indicating that the cube was a single crystal. The fringes with a lattice spacing of 0.196 nm can be indexed to the {200} planes of face-centered cubic (fcc) Rh-Pd alloy. The EDX mapping (Figure 2D and Figure S2A) shows that both Rh and Pd were distributed evenly throughout each individual Rh-Pd cube, confirming its alloy structure. This alloy structure was also confirmed by the EDX compositional line-scan recorded through an individual cube (Figure S2B). In addition, the EDX quantitative analysis taken from hundreds of cubes (Figure S2C) indicates that the atomic ratio of Rh/Pd was

about 46:54 (denoted as $\text{Rh}_{46}\text{Pd}_{54}$), which was close to the feeding ratio (1:1) of Rh to Pd salt precursor.

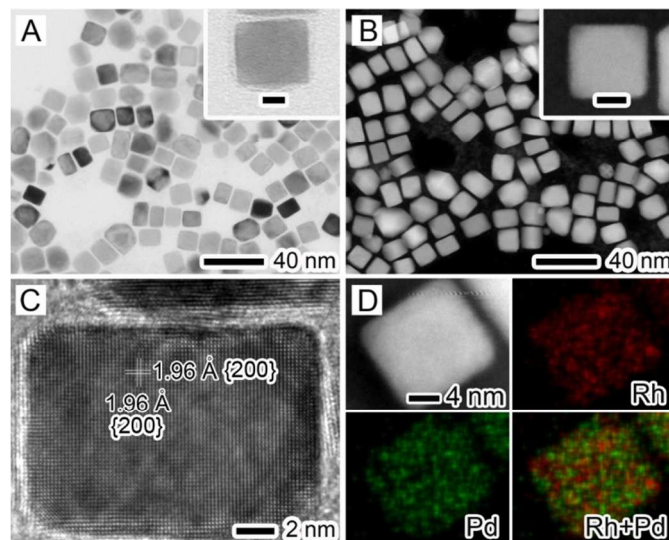


Figure 2. Morphological, structural, and compositional characterizations of Rh-Pd alloy cubes that were prepared by simultaneously injecting Na_3RhCl_6 and Na_2PdCl_4 with a molar ratio of 1:1 at a rate of 2 mL/h using a syringe pump into ethylene glycol containing ascorbic acid and KBr at 140 °C: (A) TEM image, (B) HAADF-STEM image, (C) HRTEM image, and (D) EDX mapping. The insets in (A) and (B) show TEM and HAADF-STEM images of individual nanocrystal at a higher magnification. The red and green colors in (D) correspond to Rh and Pd elements, respectively. The scale bars in the insets are 5 nm.

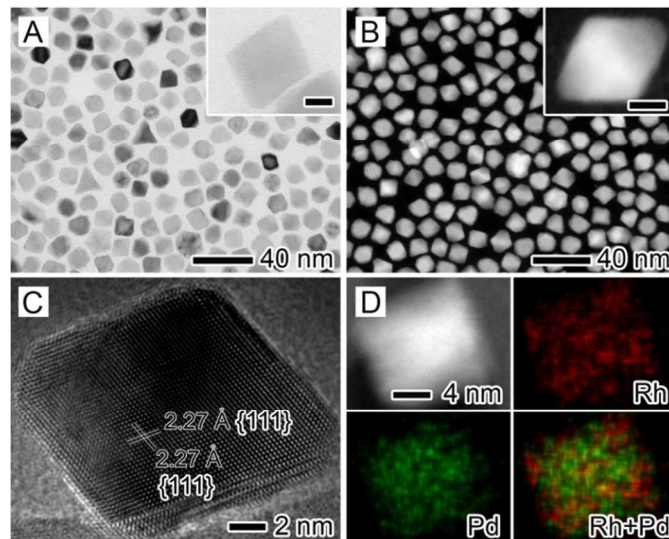


Figure 3. (A) TEM image, (B) HAADF-STEM image, (C) HRTEM image, and (D) EDX mapping of Rh-Pd alloy octahedrons that were prepared by simultaneously injecting Na_3RhCl_6 and Na_2PdCl_4 with a molar ratio of 1:1 at a rate of 2 mL/h using a syringe pump into ethylene glycol containing ascorbic acid and KBr at 120 °C. The insets in (A) and (B) show TEM and HAADF-STEM images of individual nanocrystal at a higher magnification. The red and green colors in (D) correspond to Rh and Pd elements, respectively. The scale bars in the insets are 5 nm.

Figure 3 shows structural and compositional analyses of the Rh-Pd alloy nanocrystals prepared using the standard procedure except for the different reaction temperature at 120 °C. As revealed by TEM image (Figure 3A), most of the nanocrystals (ca. 82%) were dominated by a shape of octahedron with an average edge length of 13 nm. Careful observation (inset of Figure 3A) shows that the octahedron was also slightly truncated at six corners but mainly covered by the {111} facets. The octahedral shape of the product was also clearly visualized in a HAADF-STEM image (Figure 3B). An HRTEM image (Figure 3C) taken from an individual octahedron suggests that it was a single-crystal structure with its surface enclosed by the {111} facets, which was consistent to the d-spacing lattices of 2.27 Å with an angle of 70.5°. The elemental mapping analysis in Figure 3D demonstrates that the octahedron was a binary alloy, with both Rh and Pd homogeneously distributed throughout the nanocrystal. This demonstration was also supported by the EDX mapping analysis for multiple octahedra and line-scan (Figure S3, A and B). As revealed by EDX spectrum (Figure S3C), the Rh/Pd atomic ratio of the octahedra was about 43:57 (denoted as Rh₄₃Pd₅₇). Taken together, Rh-Pd alloy cubes covered by the {100} facets and octahedra enclosed by the {111} facets were successfully generated by simultaneously injecting Rh and Pd precursors with a molar ratio of 1:1 at an extremely slow rate of 2 mL/h performed at 140 and 120 °C, respectively.

The growth behaviors associated with Rh-rich and Pd-rich crystal were systematically investigated to understand their reaction kinetics. Figure 4 shows TEM images of Rh-Pd alloy nanocrystals prepared using the standard procedure at 140 and 120 °C, respectively, except for the variation of the Rh/Pd molar ratios from 4:1 to 2:1, 1:2 and 1:4. From these TEM micrographs, it is clear that the Rh-rich samples (Figure 4, A, B, E, and F) preferred to form cubic nanocrystals, whereas, the Pd-rich ones (Figure 4, C, D, G, and H) were dominated by octahedra regardless of different reaction temperatures (e.g., 140 and 120 °C). The productivity of these two shapes in the samples was shown in Table S1. We believe that this morphology variation can be attributed to the different kinetically-controlled growth behavior associated with Rh and Pd at an extremely slow injection rate in this reaction condition.^[29,38] Due to the difficulty in dissolving Rh, EDX instead of inductively coupled plasma mass spectrometry (ICP-MS) was employed to determine the composition of the Rh-Pd alloy nanocrystals. On the basis of EDX analysis (see Figure S4, A-D), Rh₈₀Pd₂₀, Rh₆₄Pd₃₆, Rh₃₀Pd₇₀, and Rh₁₇Pd₈₃ alloy nanocrystals were obtained by varying the molar ratio of Rh to Pd salt precursors from 4:1 to 2:1, 1:2, and 1:4 added in the synthesis at 140 °C. The final composition of Rh-Pd nanocrystals is close to the feeding ratio of metal precursors. When decreasing the reaction temperature to 120 °C (see Figure S4, E-H), Rh-Pd alloy nanocrystals with similar compositions were produced except for the sample (labeled by Rh₈Pd₉₂) prepared using a Rh/Pd molar ratio of 1:4. In addition, XPS analysis was further used to characterize the surface composition of these five samples prepared at 120 °C since this parameter plays a more important role in determining the catalytic performance. (see Table S2 and Figure S5). From these data, we can conclude that the surface composition of the Rh-Pd alloy nanocrystals is almost the same as the feeding ratio of metal precursors. Figure S6 shows XRD patterns of these ten

samples with different compositions prepared at 140 and 120 °C, respectively. All the samples show four well-defined diffraction peaks that originated from a single fcc lattice. The patterns gradually shift to higher positions of 2θ with increasing the amount of Rh composition, implying the formation of alloy structure with a wide range of compositions between Rh and Pd with small lattice mismatch.

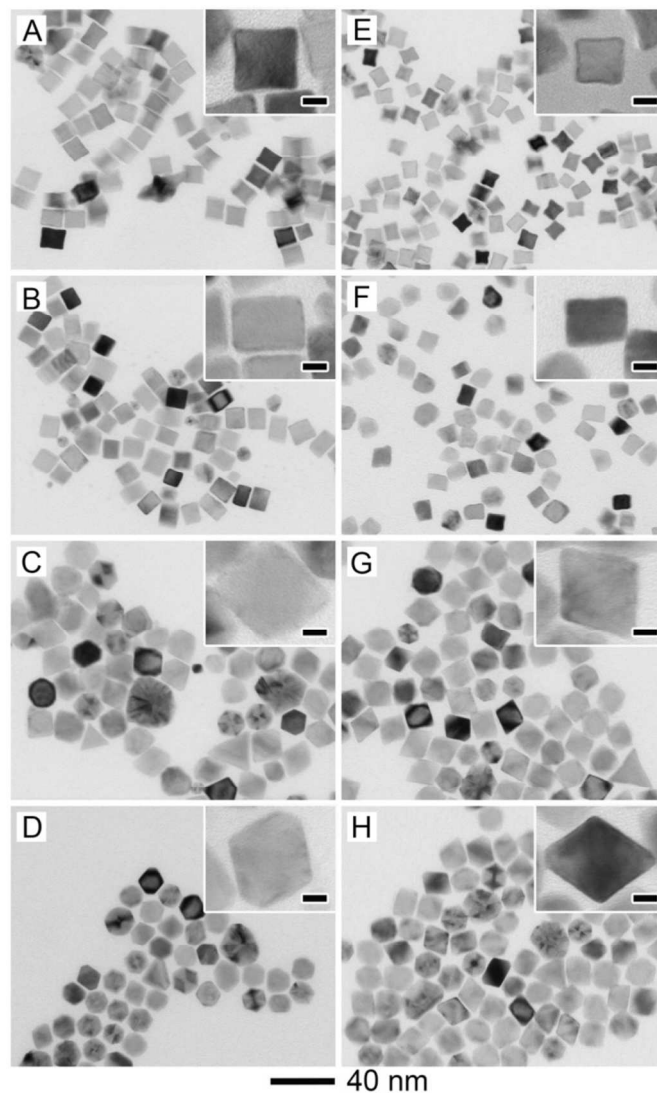


Figure 4. TEM images of Rh-Pd alloy nanocrystals that were obtained with an injection rate of 2 mL/h at 140 (A-D) and 120 °C (E-H), respectively, by varying the Rh/Pd molar ratios: (A, E) 4:1, (B, F) 2:1, (C, G) 1:2, and (D, H) 1:4. The insets show TEM images of individual nanocrystal at a higher magnification. The scale bars in the insets are 5 nm.

In order to decipher the formation mechanism of the Rh-Pd alloy cubes and octahedra, the growth behaviors associated with pure Rh and Pd under kinetic control have been clarified separately. In our previous study, Rh nanocubes and concave nanocubes were eventually generated at different injection rates.^[38] This demonstration was also confirmed by the control experiments, as shown in Figure S7. As observed, Rh concave nanocubes were generated at a slow injection rate (2 mL/h), while, Rh conventional nanocubes were formed at a fast injection rate (2.5 mL/s). This result indicates that the injection

rate has a great influence on the growth behavior of Rh nanocrystals, especially, the preferential overgrowth along the $\langle 111 \rangle$ direction by retarding the reaction kinetics. For a system involving Pd, however, retarding the reaction kinetics has a great impact on the growth behavior and thus the final shape of the nanocrystals. Figure S8A shows TEM image of Pd nanocrystals prepared by injecting Na_2PdCl_4 into the reaction at a rate of 2 mL/h and 140 °C. Interestingly, a large number of Pd triangle plates, together with a small amount of Pd decahedra were mainly bounded by the $\{111\}$ facets, indicating that the Pd $\langle 111 \rangle$ direction growth was eliminated in this reaction condition. These two shapes were confirmed by the HRTEM images (Figure S8, B and C). When the Na_2PdCl_4 solution was rapidly injected into the reaction using a pipette (ca. 2.5 mL/s), most of Pd nanocubes enclosed by the $\{100\}$ facets were eventually formed (see Figure S8D). In this case, the preferential adsorption of Br^- ions serving as a capping agent on the Pd $\{100\}$ facets led to the cubic shape, which was consistent with the conventional result under thermodynamic control.^[15] The similar growth behaviors of Pd was also observed when the reaction was conducted at 120 °C (see Figure S9). Combined together, the reason why the shape evolution of Rh-Pd alloy nanocrystals from cube to octahedron with the variation on the molar ratio of the precursors from Rh rich to Pd rich can be attributed to their different growth behaviors under sluggish growth kinetics. This demonstration was further confirmed by the results that obtained at a rapid injection rate (see Figure S10). When the reaction was conducted at a rapid injection rate (e.g., 0.5 mL/min), the cubic shape in the Pd rich samples was always generated due to the selective adsorption of Br^- ions on the $\{100\}$ facets under thermodynamic control.

For a system involving Rh and Pd with a molar ratio of 1:1, we believed that the different reduction rate between Rh and Pd salt precursors would be responsible for the different outcomes obtained at 120 and 140 °C, respectively. For this purpose, we conducted a set of experiments by separately adding Na_3RhCl_6 and Na_2PdCl_4 into the reaction and lasting for 5 min to show the difference in the reduction rate of Rh and Pd salt precursors at the afore-mentioned temperatures (see Figure S11). The color of the solution associated with Rh at 120 °C immediately turned from rose pink (the original color) to dark brown (Figure S11A), indicating the formation of Rh nanocrystals due to the rapid reduction of Na_3RhCl_6 by AA.^[38] For comparison, the Na_2PdCl_4 solution was colored by light orange after 5 min at 120 °C owing to the $[\text{PdBr}_4]^{2-}$ complex formation (Figure S11B).^[39] As such, Rh rich nanocrystals were initially generated in the nucleation stage due to the much more rapid reduction rate of Na_3RhCl_6 than the $[\text{PdBr}_4]^{2-}$ complex at this temperature. These nanocrystals then served as seeds in the subsequent growth process. In addition, the substantially large consumption of Na_3RhCl_6 for the formation of Rh rich seeds enabled the growth behavior of Rh-Pd alloy nanocrystals to adopt that of Pd due to the existence of Pd rich reaction solution, leading to the Rh-Pd alloy octahedra. This demonstration was supported by the time-dependent TEM observation (Figure S12). From these TEM images, a large number of nanocubes of 3-4 nm in size were formed in the initial stage (Figure S12A). The formation of nanocubes can probably be attributed to the preferential chemisorption of Br^- ions on Rh-rich $\{100\}$ rather than other facets.^[15] After that, these nanocubes evolved into

cuboctahedrons (Figure S12B), truncated octahedra (Figure S12C), and then octahedra (Figure S12D) by eliminating the growth along the $\langle 111 \rangle$ direction (i.e., the growth behavior of Pd in this condition) as the amount of the Rh and Pd precursors was slowly injected. When the reaction proceeded at 140 °C for 5 min, the color of the Na_3RhCl_6 and Na_2PdCl_4 solution was both dark brown (Figure S11, C and D), indicating their similar reduction rate. In this case, the Rh-Pd alloy nanocubes of 5-6 nm in size were also generated in the nucleation stage of the reaction due to the selective adsorption of Br^- ions on Rh-rich $\{100\}$ surface (Figure S13A). This growth behavior should be maintained during the overall reaction due to the almost constant molar ratio of Rh and Pd precursors in the solution. As such, cubic shape of Rh-Pd alloy nanocrystal was also kept intact with increasing sizes (Figure S13, B-D).

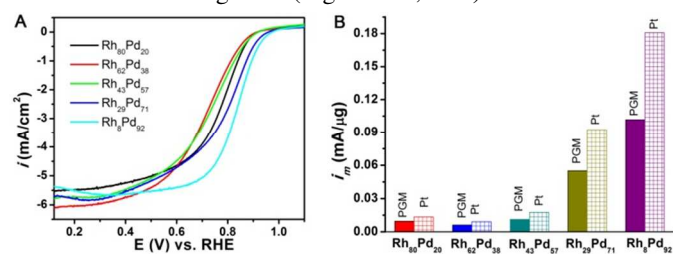


Figure 5. (a) ORR polarization curves and (b) ORR mass activities at 0.9 V of Rh-Pd cubes and octahedra.

The ORR performances of the Rh-Pd catalysts with well defined shapes, surfaces and compositions were measured on rotating disk electrode (RDE) in 0.1-M HClO_4 solution (Figure 5 and Figure S14). The ORR polarization curves of the five carbon supported Rh-Pd synthesized at 120 °C were quite different in term of the onset potential, half wave potential and slope, because these parameters in ORR activity involved the multiple effects (e.g. compositions and facets). From the Table S3, which listed all the ORR parameters among the five samples, on the $\{100\}$ facets of cube, oxygen reduction was much faster with the composition of $\text{Rh}_{80}\text{Pd}_{20}$ than that with $\text{Rh}_{62}\text{Pd}_{38}$, while the reversible trend was shown in the $\{111\}$ planes of octahedron: that is the surface with higher Pd composition is more active than that with lower Pd atomic ratios in oxygen reduction. The facet dependence of ORR activity was also studied by comparing the $\text{Rh}_{43}\text{Pd}_{57}$ octahedra made at 120 °C and the $\text{Rh}_{46}\text{Pd}_{54}$ cubes synthesized at 140 °C with the similar composition (Figure S15). The ORR area activity of the $\text{Rh}_{43}\text{Pd}_{57}$ octahedra is 150 % higher than that of the $\text{Rh}_{46}\text{Pd}_{54}$ cubes. The facet preferential ORR activity has been proved in the study of Pt based single crystal surface, because the oxygen species adsorption on the closest packed $\{111\}$ surface was weakened compared with that on $\{100\}$.^[8,40] Therefore, the oxygen reduction kinetics was improved. Thus, these facet and composition dependences of ORR on Rh-Pd catalysts leads to a fact that $\text{Rh}_8\text{Pd}_{92}$ octahedron is the most active among the five samples (Figure 5B and Table S3). The mass activity of $\text{Rh}_8\text{Pd}_{92}$ octahedron is 0.10 $\text{mA}/\mu\text{g}_{\text{PGM}}$ or 0.18 $\text{mA}/\mu\text{g}_{\text{Pt}}$ at 0.9 V by converting the mass of Rh-Pd into Pt with an equivalent cost, which is two-fold higher as that of commercial Pt/C (see Figure S16). This activity of $\text{Rh}_8\text{Pd}_{92}$ octahedron is almost equivalent to that of other Pd-based alloys (see Table S4).

A rotating-disk-electrode (RDE)-based durability study was used to evaluate the durability of Rh-Pd catalysts by

performing 30,000 potential cycles between 0.6 and 1.0 V in O₂ saturated 0.1-M HClO₄ solution. We performed 40 cycles in 0.1 M HClO₄ electrolyte before the ORR test to remove the residual surfactants on metal surface. We found that both Rh-Pd cubes and octahedra were highly stable with only less than 25 % loss in mass activity after 30,000 CV cycles with an O₂ flow (Figure 6). However, by the comparison between Rh₈₀Pd₂₀, Rh₂₉Pd₇₁ and Rh₈Pd₉₂, there was still a slight difference among these three samples. The order of the mass activity loss is Rh₈₀Pd₂₀ (19.5%) < Rh₂₉Pd₇₁ (21.6%) < Rh₈Pd₉₂ (24.7%), which indicates the ORR stability of Rh-Pd bimetallic catalysts could be improved with increase of the Rh composition, although the high Rh composition might lead to the low ORR activity. The shift of the half wave potentials shows the same trend and all the changes are within 7 mV (Figure 6, A-C). Indeed, Rh₈Pd₉₂ made at 120 °C remain ~75% of the initial activity, a mass activity of 0.075 mA/μg_{Pd}, or 0.135 mA/μg_{Pt}, which is 3.3 times as that of commercial Pt/C after ADT test for 30,000 cycles (Figure 6D and Figure S16B). Overall, Rh-Pd alloys show the substantially enhanced stability towards ORR in comparison with Pd or other Pd-based alloys (e.g., Pd-Co and Pd-Cu), which is essential to widespread applications.

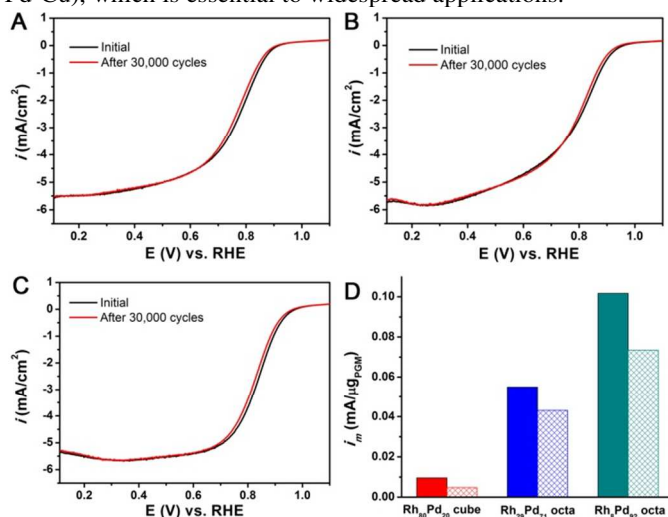


Figure 6. ORR durability tests of (A) Rh₈₀Pd₂₀ cube, (B) Rh₂₉Pd₇₁ octahedron, (C) Rh₈Pd₉₂ octahedron, and (D) comparison of ORR mass activities at 0.9 V before (solid) and after (sparse) 30,000 CV cycles.

To further clarify the role of Rh in significantly improving the electrocatalytic stability of Rh-Pd alloy nanocrystals, Pd nanocubes of 10 nm in size were synthesized according to our previous report^[41] and then evaluated as electrocatalysts towards ORR (Figure S17). Figure S17, A and B, shows CV curves and mass activities of Pd nanocubes before and after ADT test for 30,000 cycles. It is clear that Pd nanocubes show the poor ORR stability with more than 82% loss in mass activity after 30,000 cycles. TEM observation indicates that the morphology of the Pd nanocubes was completely destroyed after ADT test (Figure S17, C and D). For comparison, the octahedral morphology of Rh₈Pd₉₂ alloys almost keeps intact after 30,000 CV cycles with an O₂ flow (Figure 18). As a result, these control experiments indicate that alloying Pd with Rh is crucial to improve the stability towards ORR. It is well-known that Rh is a chemically inert metal with a high resistance to the base and acid etching.^[35] Our previous result also indicates that

pure Rh shows the superior electrocatalytic stability towards ORR.^[37] Due to the relatively lower redox potential of Rh ions relative to Pd ions (e.g., 0.915 V for Pd²⁺/Pd and 0.8 V for Rh³⁺/Rh versus RHE),^[42] Rh can be considered as a sacrificial electrode in Rh-Pd alloy nanocrystals during ORR to improve the stability. In addition, a significant electron coupling between Rh and Pd might account for the observed stabilization of Pd, which was also demonstrated in other system involving Au and Pt.^[43]

Conclusions

We have developed a facile polyol approach to the synthesis of Rh-Pd alloy cubes and octahedral with different compositions in the presence of one capping agent (i.e., Br⁻ ions) by extremely slowing down the injection rate of the precursors to manipulate the growth kinetics. The key to the success of this synthesis is the different growth behavior of Rh and Pd under sluggish kinetic control. This shape control was eventually achieved by varying the molar ratios of the Rh to Pd precursors and the reaction temperature. The incorporation of Rh into Pd-based nanocrystals can substantially enhanced the mass activity and durability towards ORR relative to commercial Pt/C, with the Rh₈Pd₉₂ alloy octahedra being the best catalysts due to the possible synergistic effects between facet and composition. This work provided an effective strategy to design faceted non-Pt ORR catalysts with enhanced the ORR catalytic performance, especially durability.

Acknowledgements

The work on microscopy was carried out in the Center for Electron Microscopy of Zhejiang University. This work is financially supported by the National Science Foundation of China (51372222, 51222202), the National Basic Research Program of China (2014CB932500), the Program for Innovative Research Team in University of Ministry of Education of China (IRT13037) and the Fundamental Research Funds for the Central Universities (2014FZA4007, 2014XZZX003-07).

Notes and references

^a State Key Laboratory of Silicon Materials, Department of Materials Science and Engineering, Key Laboratory of Advanced Materials and Applications for Batteries of Zhejiang Province, and Cyrus Tang Center for Sensor Materials and Applications, Zhejiang University, Hangzhou, Zhejiang 310027, P. R. China. Fax: 86-571-87952322; Tel: 86-571-87953190; E-mail: msezhanghui@zju.edu.cn

^b Shaanxi Materials Analysis and Research Center, School of Materials Science and Engineering, Northwestern Polytechnical University, Xi'an, Shaanxi 710072, P. R. China

[§] These authors contributed equally to this work.

† Electronic Supplementary Information (ESI) available: See DOI: 10.1039/b000000x/

- 1 G. Somorjai and Y. Li, *Proc. Natl. Acad. Sci. USA*, 2011, **108**, 917-924.
- 2 R. Van Santen, *Acc. Chem. Res.*, 2009, **42**, 57-66.
- 3 M. Crespo-Quesada, A. Yarulin, M. Jin, Y. Xia and L. Kiwi-Minsker, *J. Am. Chem. Soc.*, 2011, **133**, 12787-12794.
- 4 A. Tao, S. Habas and P. Yang, *Small*, 2008, **4**, 310-325.

- 5 J. Gu, Y. Zhang and F. Tao, *Chem. Soc. Rev.*, 2012, 41, 8050-8065.
- 6 K. Zhou and Y. Li, *Angew. Chem. Int. Ed.*, 2012, **51**, 602-613.
- 7 Z. Quan, Y. Wang and J. Fang, *Acc. Chem. Res.*, 2013, **46**, 191-202.
- 8 V. Stamenkovic, B. Fowler, B. Mun, G. Wang, P. Ross, C. Lucas and N. Markovic, *Science*, 2007, **315**, 493-497.
- 9 J. Wu, A. Gross and H. Yang, *Nano Lett.*, 2011, **11**, 798-802.
- 10 J. Zhang, H. Yang, J. Fang, and S. Zou, *Nano Lett.*, 2010, **10**, 638-644.
- 11 X. Huang, Y. Li, Y. Li, H. Zhou, X. Duan and Y. Huang, *Nano Lett.*, 2012, **12**, 4265-4270.
- 12 Y. Wu, S. Cai, D. Wang, W. He and Y. Li, *J. Am. Chem. Soc.*, 2012, **134**, 8975-8981.
- 13 A. Yin, X. Min, Y. Zhang and C. Yan, *J. Am. Chem. Soc.*, 2011, **133**, 3816-3819.
- 14 M. Chen, B. Wu, J. Yang and N. Zheng, *Adv. Mater.*, 2012, **24**, 862-879.
- 15 B. Lim, M. Jiang, J. Tao, P. Camargo, Y. Zhu and Y. Xia, *Adv. Funct. Mater.*, 2009, **19**, 189-200.
- 16 J. Zeng, Y. Zheng, M. Rycenga, J. Tao, Z. Li, Q. Zhang, Y. Zhu, Y. Xia, *J. Am. Chem. Soc.*, 2010, **132**, 8552-8553.
- 17 B. Lim, Y. Xiong and Y. Xia, *Angew. Chem. Int. Ed.*, 2007, **46**, 9279-9282.
- 18 X. Huang, S. Tang, X. Mu, Y. Dai, G. Chen, Z. Zhou, F. Ruan, Z. Yang and N. Zheng, *Nat. Nanotechnol.*, 2011, **6**, 28-32.
- 19 C. Wang, H. Daimon, Y. Lee, J. Kim and S. Sun, *J. Am. Chem. Soc.*, 2007, **129**, 6974-6975.
- 20 Y. Zhang, M. Grass, J. Kuhn, F. Tao, S. Habas, W. Huang, P. Yang and G. Somorjai, *J. Am. Chem. Soc.*, 2008, **130**, 5868-5869.
- 21 J. Wu, L. Qi, H. You, A. Gross, J. Li and H. Yang, *J. Am. Chem. Soc.*, 2012, **134**, 11880-11883.
- 22 J. Park, C. Aliaga, J. Renzas, H. Lee and G. Somorjai, *Catal. Lett.*, 2009, **129**, 1-6.
- 23 M. Crespo-Quesada, J. Andanson, A. Yarulin, B. Lim, Y. Xia and L. Kiwi-Minsker, *Langmuir*, 2011, **27**, 7909-7916.
- 24 Y. Xia, Y. Xiong, B. Lim and S. Skrabalak, *Angew. Chem., Int. Ed.*, 2009, **48**, 60-103.
- 25 A. Biacchi and R. Schaak, *ACS Nano*, 2011, **5**, 8089-8099.
- 26 H. Zhang, M. Jin and Y. Xia, *Angew. Chem. Int. Ed.*, 2012, **51**, 7656-7673.
- 27 J. Chen, T. Herricks and Y. Xia, *Angew. Chem. Int. Ed.*, 2005, **44**, 2589-2592.
- 28 C. DeSantis, A. Peverly, D. Peters and S. Skrabalak, *Nano Lett.*, 2011, **11**, 2164-2168.
- 29 C. Zhu, J. Zeng, P. Lu, J. Liu, Z. Gu and Y. Xia, *Chem. Eur. J.*, 2013, **19**, 5127-5133.
- 30 J. Zeng, C. Zhu, J. Tao, M. Jin, H. Zhang, Z. Li, Y. Zhu and Y. Xia, *Angew. Chem. Int. Ed.*, 2012, **51**, 2354-2358.
- 31 E. Antolini, *Energy Environ. Sci.*, 2009, **2**, 915-931.
- 32 B. Adams and A. Chen, *Mater. Today*, 2011, **14**, 282-289.
- 33 M. Shao, *J. Power Source*, 2011, **196**, 2433-2444.
- 34 J. Handley, *Platinum Metals Rev.*, 1989, **33**, 64-72.
- 35 S. Xie, N. Lu, Z. Xie, J. Wang, M. Kim and Y. Xia, *Angew. Chem., Int. Ed.* 2012, **51**, 10266-10270.
- 36 B. Sneed, C. Kuo, C. Brodsky and C. Tsung, *J. Am. Chem. Soc.*, 2012, **134**, 18417-18426.
- 37 Y. Qi, J. Wu, H. Zhang, Y. Jiang, C. Jin, M. Fu, H. Yang and D. Yang, *Nanoscale*, 2014, **6**, 7012-7018.
- 38 H. Zhang, W. Li, M. Jin, J. Zeng, T. Yu, D. Yang and Y. Xia, *Nano Lett.*, 2011, **11**, 898-903.
- 39 M. Jin, H. Zhang, Z. Xie and Y. Xia, *Angew. Chem. Int. Ed.*, 2011, **50**, 7850-7854.
- 40 V. Stamenkovi, B. Mun, K. Mayrhofer, P. Ross, N. Markovic, J. Rossmeisl, J. Greeley and J. Nørskov, *Angew. Chem. Int. Ed.*, 2006, **46**, 2897-2901.
- 41 M. Jin, H. Liu, H. Zhang, Z. Xie, J. Liu and Y. Xia, *Nano Res.* 2011, **4**, 83-91.
- 42 C. Zoski, *Handbook of Electrochemistry*, Elsevier, Oxford, 2006, vol. 18, p. 817.
- 43 J. Zhang, K. Sasaki, E. Sutter and R. Adzic, *Science* 2007, **315**, 220-222.